



저작자표시-비영리-변경금지 2.0 대한민국

이용자는 아래의 조건을 따르는 경우에 한하여 자유롭게

- 이 저작물을 복제, 배포, 전송, 전시, 공연 및 방송할 수 있습니다.

다음과 같은 조건을 따라야 합니다:



저작자표시. 귀하는 원저작자를 표시하여야 합니다.



비영리. 귀하는 이 저작물을 영리 목적으로 이용할 수 없습니다.



변경금지. 귀하는 이 저작물을 개작, 변형 또는 가공할 수 없습니다.

- 귀하는, 이 저작물의 재이용이나 배포의 경우, 이 저작물에 적용된 이용허락조건을 명확하게 나타내어야 합니다.
- 저작권자로부터 별도의 허가를 받으면 이러한 조건들은 적용되지 않습니다.

저작권법에 따른 이용자의 권리는 위의 내용에 의하여 영향을 받지 않습니다.

이것은 [이용허락규약\(Legal Code\)](#)을 이해하기 쉽게 요약한 것입니다.

[Disclaimer](#)

공학석사학위논문

**Fabrication of Urchin-like PANI/RGO/PPy
Nanocomposite for Supercapacitor Electrode**

성계 구조 폴리아닐린/환원된 그래핀 산화물/폴리피롤
나노복합체의 제조와 슈퍼커패시터 전극 응용

2016년 2월

서울대학교 대학원

화학생물공학부

김 지 후

<p>Fabrication of Urchin-like PANI/RGO/PPy Nanocomposite for Supercapacitor Electrode</p>		<p>2016</p>	<p>김지후</p>
<p>↑ 2cm ↓</p>		<p>↑ 2.5cm ↓</p>	<p>↑ 4cm ↓</p>
		<p>↑ 3cm ↓</p>	<p>↑ 2cm ↓</p>

Fabrication of Urchin-like PANI/RGO/PPy Nanocomposite for Supercapacitor Electrode

지도 교수 장 정 식

이 논문을 공학석사 학위논문으로 제출함
2016 년 2 월

서울대학교 대학원
화학생물공학부
김 지 후

김지후의 석사 학위논문을 인준함
2016 년 2 월

위 원 장 _____ (인)

부위원장 _____ (인)

위 원 _____ (인)

Abstract

Fabrication of Urchin-like PANI/RGO/PPy Nanocomposite for Supercapacitor Electrode

Jihoo Kim

School of Chemical and Biological Engineering

The Graduate School

Seoul National University

Urchin-like polyaniline/polypyrrole/reduced graphene oxide composite was synthesized through a self-stabilized dispersion polymerization method. When applied to electrode materials for aqueous supercapacitors, the composite exhibits a high specific capacitance of *ca.* 350 F g⁻¹ at a current

density of *ca.* 0.5 A g^{-1} as well as good rate capability (keeping *ca.* 78 % of the initial value after 1000 cycles at a current density of *ca.* 0.5 A g^{-1}). The enhancement of electrochemical performances might be attributed to the synergistic effects between graphene and urchin-like polyaniline/polypyrrole components with an improved specific surface area and electrical conductivity.

Keyword: Polyaniline, Reduced graphene oxide, Polypyrrole, Supercapacitor.

Student number: 2014-20629

List of Abbreviations

PANI: Polyaniline

RGO: Reduced Graphene Oxide

PPy: Polypyrrole

APS: Ammonium Persulfate

BET: Brunauer–Emmett–Teller

FE-SEM: Field-Emission Scanning Electron Microscope

XPS: X-ray Photoelectron Spectroscopy

XRD: X-ray Diffraction Spectroscopy

CV: Cyclic Voltammetry

List of Figures

Figure 1. Schematic illustration of the fabrication of PANI/RGO/PPy using a self-stabilized dispersion polymerization method.

Figure 2. SEM images of (a) RGO, (b) RGO/PPy, and (c) PANI/RGO/PPy (PPy: 0.3 wt%). Respective insets show enlarged SEM images (scale bar = 100 nm).

Figure 3. SEM images of prepared (a) PANI/RGO and PANI/RGO/PPy with (b) 0.1 wt%, (c) 0.3 wt% of PPy (scale bar= 1 μ m).

Figure 4. Nitrogen adsorption/desorption isotherms of PANI/RGO/PPy (PPy: 0.1 and 0.3 wt%) and PANI/RGO.

Figure 5. XPS spectra of PANI/RGO/PPy, RGO/PPy, and RGO (PPy: 0.3 wt%).

Figure 6. XRD patterns of PANI/RGO/PPy and (a) RGO/PPy and RGO; (b) PANI/RGO and PANI; (c) PANI/RGO and PANI/RGO/PPy with different PPy concentrations: 0.1, 0.2, and 0.3 wt%.

Figure 7. (a) CV curves for PANI/RGO/PPy, PANI/PPy, and RGO. (b) CV curves for PANI/RGO/PPy at different scan rates. (c) Galvanostatic charge/discharge profiles for PANI/RGO/PPy, PANI/PPy, and RGO. (d) Capacitance retention plot of PANI/RGO/PPy and PANI with cycle number (PPy: all 0.3 wt%).

List of Tables

Table 1. BET surface areas and total pore volumes of pristine RGO, RGO/PPy, and PANI/RGO/PPy (PPy: 0.3 wt%).

Table 2. BET surface areas and total pore volumes of PANI/RGO and PANI/RGO/PPy with different PPy concentrations.

Table 3. The elemental composition of pristine RGO, pristine PPy, RGO/PPy and PANI/RGO/PPy composite (PPy: 0.3 wt%) as measured by XPS analysis. The values were calculated in atomic percent.

Contents

Abstract.....	i
List of Abbreviations.....	iii
List of Figures.....	iv
List of Tables.....	v
Contents	vi
Chapter 1. Introduction	1
1.1 Supercapacitors	1
1.1.1 Design strategies for supercapacitors	3
1.1.2 Advantages of urchin-like structures	4
1.2 Graphene	5
1.3 Transition metal oxides	6
1.4 Polyaniline and its composites.....	7
1.5 Objective of this study	8
Chapter 2. Experimental.....	9
2.1 Materials	9
2.2 Preparation of RGO	10
2.3 Preparation of PPy	11
2.4 Fabrication of PANI/RGO/PPy	11

2.5	Control experiments.....	12
2.5.1	Fabrication of PANI.....	12
2.5.2	Fabrication of PANI/RGO.....	13
2.5.3	Fabrication of PANI/PPy.....	14
2.6	Characterization.....	15
Chapter 3. Results and discussion.....		17
3.1	Synthesis of the PANI/RGO/PPy.....	17
3.2	Characterization of the PANI/RGO/PPy.....	20
3.2.1	Morphology and related properties.....	20
3.2.2	Further investigation of synthesis.....	28
3.3	Investigation of crystallinity.....	32
3.4	Investigation of electrochemical performance.....	35
Chapter 4. Conclusion.....		39
References.....		40
국문초록.....		44

Chapter 1. Introduction

1.1 Supercapacitors

Recently, electrical energy storage and conversion systems have been significantly investigated due to the environmental issues such as depletion of fossil fuels and grave climate change [1]. Among the systems, supercapacitors have drawn continuous attention in recent decades owing to their long cycle life, fast charge–discharge processes, long lifespan, and low maintenance cost [2].

Supercapacitors can be generally classified into two categories on the basis of their charge storage mechanisms, the electrochemical double layer capacitors and pseudocapacitors [3]. Electrochemical double layer capacitors physically store charges through charge separation with reversible ion adsorption at the interface between electrode and electrolyte [4]. Meanwhile, pseudocapacitors chemically store the charges via Faradaic redox reactions within a few nanometers of the electrode materials [5].

Because the specific capacitance of supercapacitor depends upon the electrical charge stored at the interface between the electrolyte and electrode materials, electrode materials for electrical double layer capacitors generally

use carbon-based materials with high specific surface area, including carbon nanotubes, activated carbon, and graphene [6]. The electrical double layer capacitors can offer high charge-discharge rates with long cycling stability, while a low specific capacitance of carbon materials (typically less than 200 F g⁻¹) limits their practical application [7]. Conversely, pseudocapacitors can provide superior specific capacitance. However, pseudocapacitive materials suffer from their respective problems: the low electrical conductivity and high cost for transition metal oxide and poor cycling stability due to their mechanical degradation for conducting polymers [8]. To overcome these drawbacks, hybrid supercapacitor electrodes have been produced with an expectation to take advantage of both types of electrodes for highly efficient energy storage [9].

1.1.1 Design strategies for supercapacitors

In order to produce an effective supercapacitor electrode, an engineer should consider three criteria: good rate capability, retaining an acceptable capacitance even at the high scan rate, good cycling stability, and, of course, high capacitance [10]. Additionally, the possibility of toxicity and overall cost for production should be included [11]. Recent studies have shown that specific surface area, electronic and ionic conductivity are main factors to satisfy the criteria. (1) Ionic and electronic conductivity: Both factors affect the specific capacitance and stability, and they are crucial to retain a rectangular cyclic voltammogram and symmetric galvanostatic charge-discharge curves. At higher scan rates, they help to maintain a low specific capacitance losses [12]. Therefore, to enhance the ionic conductivity, it is imperative to design an open nanostructures, with tuning pore size, for transportation of ions. (2) Specific surface area: The higher specific surface area indicates the copious charges stored in the proximity of the electrode materials, implying the enhanced specific capacitance of the material [13]. (3) Electrochemical stability. During the electrochemical tests, due to the side reaction, dissolution, contaminants, and phase change itself, the electrochemical, namely mechanical and chemical, cyclic performance are reduced [14].

1.1.2 Advantages of urchin-like structures

The performances of nanostructure are estimated by three standards: large capacity, high stability, and efficient kinetics [15]. These aims are pursued by the manipulation of nanostructure with electrochemically effective materials, including carbonaceous substances, metal oxides, and conducting polymers [16]. Studies have shown that urchin-like nanostructure of the materials can be effectively crystallized, which allows to maintain high cycling stability [17]. Furthermore, urchin-like nanostructures, generally made by transition metal oxides, have shown that they can provide enhanced porosity and crystallinity, implying the valuable distribution of pore size, adequate pore length and network [18]. These factors can offer an improved electroactive surface area with effective accession of electrolyte ions, leading to an enhanced Faradic redox reactions with suitable charge separation [19]. In addition, improved kinetics of electrolyte ions are efficiently achieved by urchin-like architecture with short path lengths for transfer of ions and electrons [20]. The effect can facilitate the enhanced cycling performance and retention at high scan rates [21].

1.2 Graphene

Graphene is a two-dimensional structure with a honeycomb lattice with high thermal conductivity and electron mobility [22]. The single-layered carbon nanomaterials possess theoretical specific surface area ($2630 \text{ m}^2 \text{ g}^{-1}$), indicating that the graphene can store plentiful charges within the interfaces [23]. The capability, together with the remarkable electric conductivity and mechanical flexibility and strength, facilitates efficient electron transfer without cyclic decay [24]. However, namely the π - π stacking, the aggregation, induced by van der Waals forces, decrease the accessible surface area with decreased porosity, as shown in Figure 1, resulting in the poor specific capacitance (*ca.* 110 F g^{-1} in alkaline electrolyte) [25]. Therefore, it remains a challenge to overcome the agglomeration and restacking of graphene sheets.

1.3 Transition metal oxides

Recently, transition metal oxides, useful pseudocapacitive materials for capacitors, have revealed great specific capacitance than electronic double layer capacitance materials, owing the reversible and fast Faradic reactions [26]. The transition metal oxides, including Co_3O_4 , NiO, TiO_2 , VO_x , MnO_2 , ZnO, and RuO_2 , however, possess some drawbacks like expensiveness or low electrical conductivity [27]. For instances, RuO_2 , boasting superb specific capacitance ($1,340 \text{ F g}^{-1}$), are expensive nanomaterials, valued at around 100 USD per gram, which hinders commercial and industrial usefulness [28]. The other transition metal oxides, such as NiO, MnO_2 , Co_3O_4 and ZnO, have been proposed to substitute that high-priced material, but they suffer from their lower specific capacitance, due to their low electrically conductive nature [29].

1.4 Polyaniline and its composites

Conducting polymers, in addition to the transition metal oxides, can provide pseudocapacitance with a fast redox reactions, but entailing a faster cyclic decay due to their poor electrochemical strength as well [30]. Among the conducting polymers, polyaniline (PANI) have been widely researched due to their efficient redox reaction with unique doping/dedoping process, economic and facile synthesis, and low cost [31]. Thankfully, blending with carbon-related materials, like graphene, can be proven to provide enhanced electrochemical properties with improved ionic and electronic transfer *via* synergistic effects of both materials [32]. The size and proportion of both materials, the existence and characteristics of functional groups on graphene sheets, proportion and contents of doping in graphene and polyaniline backbones can affect the performance of incorporated electrode materials [33]. Moreover, the performance of the composite are dependent upon the nanostructure, which can directly influence the porosity, specific surface area, and ion and electron transfer [34]. Although the urchin-like structures have been synthesized from many metal oxides, the controllable synthesis of polyaniline with the nanostructure still remains a noticeable challenge.

1.5 Objective of this study

We herein report a method combining urchin-like structured PANI/PPy onto the substrate of RGO. With the synergistic effects of PANI, PPy, graphene, fabricated composites represent the substantial enhancement of the electrochemical performances. Firstly, the inefficient utilization of graphene sheets due to the π - π stacking is overcome by the employment of PPy onto the sheets. PPy nanoparticles prevents re-stacking of graphene sheet *via* intercalation of PPy, leading to increase in the surface area of graphene sheets. Furthermore, the resulting urchin-like shaped PANI further enlarges the specific surface area of the composite. Secondly, good electrical conductivity is achieved due to PANI, synthesized by a self-stabilized dispersion polymerization method, and carbon-based backbone, resulting in the high specific capacitance. Finally, cycling stability is also enhanced owing to the advantages of graphene. The results of nitrogen adsorption-desorption experiments and electrochemical measurements demonstrate that obtained products have a large specific surface area and good electrochemical performances.

Chapter 2. Experimental

2.1 Materials

Graphite (powder, <20 μm , synthetic), sodium nitrate (NaNO_3 , reagent grade), aniline ($\text{C}_6\text{H}_7\text{N}$, $\geq 99.5\%$), ammonium persulfate (APS; $[\text{NH}_4]_2\text{S}_2\text{O}_8$, 98.0 %), potassium persulfate ($\text{K}_2\text{S}_2\text{O}_8$, $\geq 99.0\%$), hydriodic acid (HI, 57 wt.%), Poly(vinyl alcohol) (PVA, Mw: 9000), FeCl_3 (97%), and pyrrole (98 %) monomer were acquired from Sigma-Aldrich Co. (St. Louis, MO, USA). Concentrated sulfuric acid (H_2SO_4 , 95.0 %), hydrochloric acid (HCl, 37 %), hydrogen peroxide solution (H_2O_2 , 34.5 %), ammonium hydroxide (28.0–30.0 %, reagent grade), potassium permanganate (KMnO_4 , 99.3 %), sodium bicarbonate (NaHCO_3 , 99.0 %), acetic acid ($\text{CH}_3\text{CO}_2\text{H}$, 99.5 %) and chloroform (CHCl_3 , 99.5 %) were obtained from Samchun Pure Chemical Co., Ltd. (Seoul, South Korea). Absolute ethanol ($\text{C}_2\text{H}_5\text{OH}$, HPLC grade) was purchased from Fisher Scientific Korea Ltd. (Seoul, South Korea). Phosphorus pentoxide (P_2O_5) was obtained from Junsei Chemical Co., Ltd. (Tokyo, Japan). All reagents and materials were used as received without additional purification.

2.2 Preparation of RGO

RGO sheets were prepared from natural graphite powders using modified Hummers and Ruoff methods [35,36]. At the first step, graphite (1.0 g) was mixed with a solution containing H_2SO_4 (6 mL) and NaNO_3 (0.5 g). After the mixture was vigorously stirred for 30 min at 0 °C, then KMnO_4 (3.0 g) was slowly added to the solution over 1 h with stirring at the same temperature. Successively, the mixture was kept at 35 °C for 2 h, followed by the addition of deionized water (46 mL). Then the mixture was heated at 98 °C for 15 min. The resulting brownish gray paste was turned to a yellowish one after H_2O_2 solution (2.5 mL, 30%) and deionized water (130 mL) were added at 20 °C. Finally, the paste was washed initially with HCl (5 wt.%), and then with deionized water until the pH reached 7. After dried overnight, the paste was dispersed in acetic acid (200 mL), being exfoliated with sonication for 1 h. Subsequently, hydriodic acid (4 mL) was injected and stirred at 40 °C for 24 h. The resulting RGO dispersion was deposited on a cellulose acetate filter (Whatmann Inc., USA) using a vacuum filtration process. The product was washed with a NaHCO_3 solution (250 mL), water (500 mL), and acetone (250 mL) to remove excess hydriodic acid and residual iodine. The as-synthesized RGO product was dried at 20 °C for 24 h in a vacuum oven.

2.3 Preparation of PPy

Uniformly sized PPy nanoparticles with sizes of 100 nm were prepared by dispersion polymerization, as described in our previous report [37]. In a typical synthesis, poly(vinyl alcohol); PVA (9.0 wt %) was dissolved into DI water as a stabilizer, then FeCl_3 was added and mixed as an oxidizing agent (FeCl_3 : pyrrole monomer = 2.3: 1 by molar ratio). After equilibrium was reached, the pyrrole monomer was injected into PVA/ FeCl_3 solution at 0°C. The mixture rapidly turned dark, suggesting the polymerization of PPy. The resulting PPy nanoparticles were subsequently washed with water and dried overnight. For further characterization, the FE-SEM images were taken to measure the diameters of the products.

2.4 Fabrication of PANI/RGO/PPy

Initially, as-prepared PPy (0.05 g) was stirred in deionized water (10 g) for 1 h at 60 °C. Meanwhile, hydrochloric acid (5.0 g), aniline (1.0 g), as-synthesized RGO (0.05 g), and deionized water (20 g) were mixed in a vial. Subsequently, two mixtures were sonicated independently at 20 °C for 30 min., then combined and stirred at 400 rpm for 2 h at 20 °C to obtain RGO/PPy composite. Afterwards, chloroform (60 mL) was added and the

mixture was stirred for 10 min. at 20 °C. Meanwhile, a solution of APS was prepared by mixing APS (1.2 g), deionized water (10 g), and hydrochloric acid (3.0 g). The temperature of the mixture was set at -40 °C with stirring, and the temperature drop of mixture was measured thoroughly by electric thermometer. When the temperature was decreased under -9 °C, as-prepared ammonium persulfate solution was introduced in the mixture as an oxidizing agent. After the reaction was conducted at -40 °C for 24 h, PANI was synthesized on the surface of the RGO/PPy composite. We used the self-stabilized dispersion polymerization method to promote the para-direction polymerization of aniline, which results in higher conductivity than conventional methods [38]. Furthermore, the hydrophobic part of the anilinium hydrochloride (phenyl group) could be adsorbed onto the aromatic structure of the RGO by the π - π stacking interactions [39]. As a result of the fabricating procedure described herein, highly conductive and thermally robust PANI/RGO/PPy composite was produced.

2.5 Control experiments

2.5.1 Fabrication of PANI

At first, hydrochloric acid (5.0 g), aniline (1.0 g), and deionized water

(30 g) were mixed in a vial. Afterwards, chloroform (60 mL) was added and the mixture was stirred for 10 min. at 20 °C. Meanwhile, a solution of APS was prepared by mixing APS (1.2 g), deionized water (10 g), and hydrochloric acid (3.0 g). The temperature of the mixture was set at -40 °C with stirring, and the temperature drop of mixture was measured thoroughly by electric thermometer. When the temperature was decreased under -9 °C, as-prepared ammonium persulfate solution was injected in the mixture as an oxidizing agent. After the reaction was conducted at -40 °C for 24 h, PANI was synthesized.

2.5.2 Fabrication of PANI/RGO

Initially, hydrochloric acid (5.0 g), aniline (1.0 g), as-synthesized RGO (0.05 g), and deionized water (30 g) were mixed in a vial. Subsequently, the mixture was sonicated at 20 °C for 30 min., then stirred at 400 rpm for 2 h at 20 °C. Successively, chloroform (60 mL) was added and the mixture was stirred for 10 min. at 20 °C. Meanwhile, a solution of APS was prepared by mixing APS (1.2 g), deionized water (10 g), and hydrochloric acid (3.0 g). The temperature of the mixture was set at -40 °C with stirring, and the temperature drop of mixture was measured thoroughly by electric thermometer. When the temperature was decreased under -9 °C, as-prepared

ammonium persulfate solution was introduced in the mixture as an oxidizing agent. After the reaction was conducted at $-40\text{ }^{\circ}\text{C}$ for 24 h, PANI nanofibers were synthesized on the surface of the RGO sheets.

2.5.3 Fabrication of PANI/PPy

Initially, as-prepared PPy (0.05 g) was stirred in deionized water (10 g) for 1 h at $60\text{ }^{\circ}\text{C}$. Meanwhile, hydrochloric acid (5.0 g), aniline (1.0 g) and deionized water (20 g) were mixed in a vial. Subsequently, two mixtures were sonicated independently at $20\text{ }^{\circ}\text{C}$ for 30 min., then combined and stirred at 400 rpm for 2 h at $20\text{ }^{\circ}\text{C}$. Afterwards, chloroform (60 mL) was added and the mixture was stirred for 10 min. at $20\text{ }^{\circ}\text{C}$. Meanwhile, a solution of APS was prepared by mixing APS (1.2 g), deionized water (10 g), and hydrochloric acid (3.0 g). The temperature of the mixture was set at $-40\text{ }^{\circ}\text{C}$ with stirring, and the temperature drop of mixture was measured thoroughly by electric thermometer. When the temperature was decreased under $-9\text{ }^{\circ}\text{C}$, as-prepared ammonium persulfate solution was injected in the mixture as an oxidizing agent. After the reaction was conducted at $-40\text{ }^{\circ}\text{C}$ for 24 h, PANI was synthesized on the surface of the PPy.

2.6 Characterization

The morphology of the nanostructure was investigated with a Field-Emission scanning electron microscope (FE-SEM). The FE-SEM images were taken with a SUPRA 55VP (Carl Zeiss, Germany). Brunauer–Emmett–Teller (BET) measurements were conducted with an ASAP 2010 analyzer (Micromeritics, USA). All samples were measured in a liquid nitrogen bath at 77.30 K. X-ray photoelectron spectroscopy (XPS) experiments were performed using an AXIS-His electron spectrometer (Kratos, Japan) and X-ray diffraction measurements (XRD) were conducted with a D8 Advance diffractometer (Bruker, Germany) operating with monochromated Cu K α 1 radiation ($\lambda = 1.54 \text{ \AA}$). The electrical conductivity was obtained by four-point probe technique (Mode Systems Co., Korea) equipped with a Keithley 2400 current source (Keithley Co., USA). The electrical conductivity in S cm^{-1} , σ , is defined as follows: $\sigma = 1/\rho = (\ln 2/\pi t)(1/R)$, where ρ is the static resistivity in $\Omega \text{ cm}$, t is the thickness in cm and R is the surface resistance in Ω . The electrochemical performance was evaluated using galvanostatic charge/discharge measurements in a three-electrode cell system at 20 °C on an Autolab PGSTAT 302N Electrochemical Workstation. The measurements were conducted with three-electrode cells at potentials in the range 0–0.8 V versus a saturated calomel electrode (SCE) in

a 1 M H₂SO₄ aqueous solution.

Chapter 3. Results and discussion

3.1 Synthesis of the PANI/RGO/PPy.

The overall procedure for PANI/RGO/PPy is illustrated in Figure 1. In the process, PPy was directly dispersed as a nucleating agent onto the RGO, followed by the polymerization of PANI below -40 C for utilizing the self-stabilized dispersion polymerization, which enabled the growth of PANI nanoneedles onto the surface of PPy and RGO. For the preparation of the resulting composite, the PPy and RGO were produced in advance as substrates. Direct control of the PPy was achieved by the variation of PPy feed ratios (0.1–0.3 wt %) during the injection of PPy on the dispersion of RGO. The PPy was obtained using a chemical oxidation polymerization. The average diameters of PPy was *ca.* 100 nm. On the other hand, RGO was prepared using a modified Hummer's method, followed by the reduction using hydriodic acid to produce RGO. The size of prepared RGO was *ca.* 10 nm. The PPy was dispersed and stacked onto RGO sheets *via* π - π interactions, leading to RGO/PPy. Afterwards, aniline monomers were interacting with PPy and RGO by phenyl rings in the anilinium chloride form. With APS as an initiator, PANI was polymerized onto the PPy

nanoparticles, leading to PANI/PPy. Meanwhile, PANI nanoniddles were also formed on the basal plane of RGO to yield PANI/RGO. Since the PPy were already attached onto the RGO, resulting structure could be described that urchin-like PANI/PPy was dispersed on the PANI/RGO sheets.

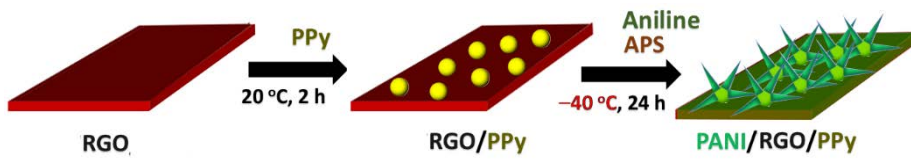


Figure 1. Schematic illustration of the fabrication of PANI/RGO/PPy using a self-stabilized dispersion polymerization method.

3.2 Characterization of the PANI/RGO/PPy

3.2.1 Morphology and related properties

The morphology of the PPy, RGO/PPy and PANI/RGO/PPy were examined using FE-SEM. Figure 2a exhibits pristine PPy, which were approximately 100 nm in size with a narrow size distribution. As shown in Figure 2b, the PPy clearly attached to the RGO with minimal aggregation. Inset presents that PPy were stacked onto the both sides of RGO. Figure 2c presents that the resulting PANI/PPy was urchin-like structure. The diameter of the structure was *ca.* 500 nm. Note that the nanostructure displayed voids and cavities, which provides an increased specific surface area for exposure to ions, with a deep ion penetration length. The urchin-like PANI/PPy architecture might facilitate charge transfer interaction between the PANI/PPy balls and RGO sheets accommodates charge transfer as well [40].

Table 1 summarizes the respective effects of PPy and RGO using BET method. Adding PPy onto the RGO results in the three times higher specific surface area than pristine RGO due to the inhibition effect of the PPy, and PANI further increase the specific surface area of overall structure. Note that RGO enables to increase specific surface area of PANI (Table 2), but the agglomeration and blockage effects on the RGO/PPy structure hamper the

further improvement of the overall specific surface area.

In order to determine the effects of PPy on urchin-like structure, the concentrations of PPy were differed in the fabrication processes. Figure 3 displays PANI/RGO/PPy with 0.1 and 0.3 wt% of PPy and PANI/RGO for comparison. BET method was also conducted to calculate the specific surface area and analysis of morphology. Hysteresis loops of the respective samples, as shown in Figure 4, point out that PPy enables mesoporous structure of overall PANI/RGO/PPy. Table 2 presents the resulting specific surface area. Among the samples, PANI with 0.3 wt% PPy are larger specific surface area ($39.55 \text{ m}^2 \text{ g}^{-1}$) than any others. The results are 1.6 times higher than that of PANI/RGO ($23.75 \text{ m}^2 \text{ g}^{-1}$). It is noticeable that the increment of PPy concentration on the synthetic process causes almost same numbers of addition in the specific surface area.

Due to the urchin-like structure of the PANI, the fabricated PANI/RGO/PPy possessed an enhanced specific surface area compared with the counterparts (Table 2 and Figure 4). Furthermore, the composite showed high electrical conductivity. The PANI/RGO/PPy had a conductivity of *ca.* 24.0 S cm^{-1} , implying that surface of the PPy was completely sealed with the PANI and RGO in accordance with the XPS results. These results were attributed to the synergetic effects of RGO with 1) PPy and 2) PANI: 1) the PPy could increase the surface area of the RGO by preventing the self-restacking of the RGO (Table 1). Thus, PANI/RGO/PPy showed a higher

specific surface area than PANI/RGO; 2) the PPy could serve as nucleation sites for the growth of PANI, inducing urchin-like structure (Figure 2). For the reason, PANI/RGO/PPy also had a larger specific surface area than PANI/RGO (Table 2)

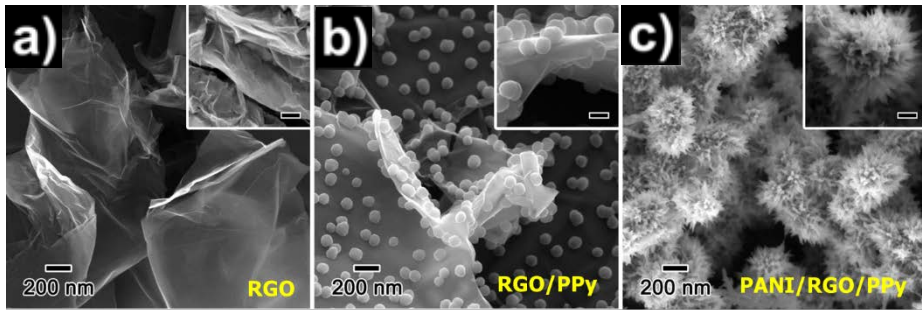


Figure 2. SEM images of (a) RGO, (b) RGO/PPy, and (c) PANI/RGO/PPy (PPy: 0.3 wt%). Respective insets show enlarged SEM images (scale bar = 100 nm).

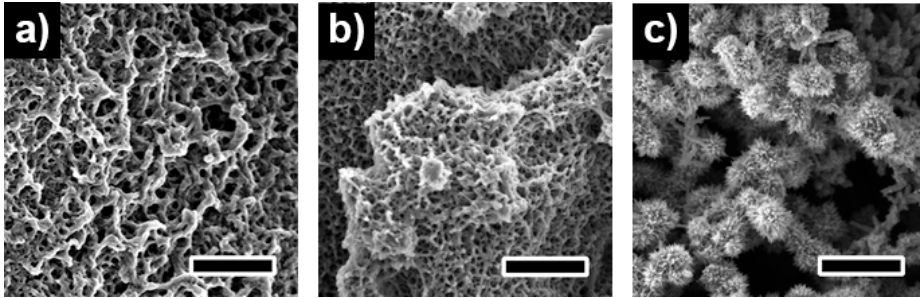


Figure 3. SEM images of prepared (a) PANI/RGO and PANI/RGO/PPy with (b) 0.1 wt%, (c) 0.3 wt% of PPy (scale bar= 1 μm).

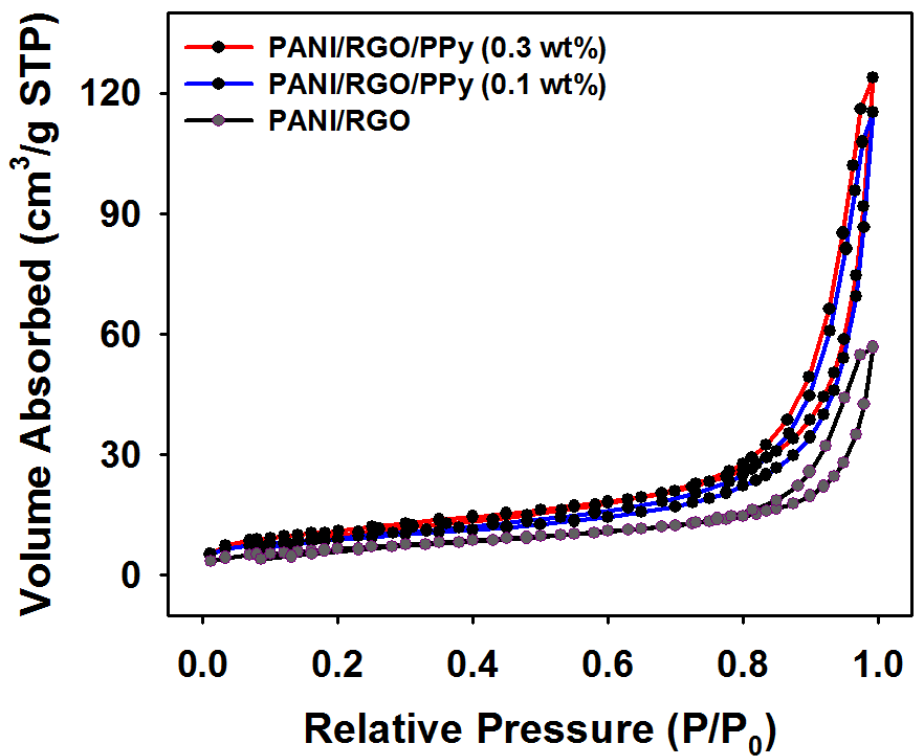


Figure 4. Nitrogen adsorption/desorption isotherms of PANI/RGO/PPy (PPy: 0.1 and 0.3 wt%) and PANI/RGO.

Table 1. BET surface areas and total pore volumes of pristine RGO, RGO/PPy, and PANI/RGO/PPy (PPy: 0.3 wt%).

Sample	Surface area (m ² g ⁻¹)	Total pore volume (cm ³ g ⁻¹)
Pristine RGO	11.13	0.067
RGO/PPy	30.10	0.207
PANI/RGO/PPy	39.55	0.184

Table 2. BET surface areas and total pore volumes of PANI/RGO and PANI/RGO/PPy with different PPy concentrations.

Sample	Surface area (m ² g ⁻¹)	Total pore volume (cm ³ g ⁻¹)
Pristine PANI	12.82	0.062
PANI/RGO	23.75	0.085
PANI/RGO/PPy (0.1 wt%)	31.45	0.175
PANI/RGO/PPy (0.2 wt%)	35.45	0.183
PANI/RGO/PPy (0.3 wt%)	39.55	0.184

3.2.2 Further investigation of synthesis

Figure 5a exhibits that X-ray photoelectron spectroscopy (XPS) analyses used to evaluate the elemental composition of the as-prepared pristine PPy, RGO/PPy, and PANI/RGO/PPy. The spectrum for the pristine PPy featured several peaks; those at 284 and 400 eV correspond to C 1s and N 1s, respectively [41]. An additional peak was found at 532 eV, which is attributed to O 1s from the addition of poly(vinyl alcohol) (PVA; $[\text{CH}_2\text{CH}(\text{OH})]_n$) stabilizer during the preparation of PPy. Although PVA could be washed *via* centrifugation, residual PVA containing hydroxyl groups was entangled with the PPy backbone due to the hydrogen bonding with the nitrogen atoms of PPy [42]. Fortunately, PVA is fairly soluble in water, thus the problem does not significantly effective on the fabrication of PANI/RGO/PPy. After PPy was stacked onto the RGO, the O peak at 531 eV, became weaker than for the pristine PPy, whereas the N 1s peak at 400 eV became more pronounced, meaning that the PPy were successfully stacked on the basal planes of RGO. As shown in the XPS spectrum of PANI/RGO/PPy composite, the C peak and N 1s peak for PANI/RGO/PPy increased substantially, whereas the O peak decreased significantly, indicating that the surface of the RGO/PPy was entirely covered by the

PANI. The precise elemental composition of each sample is summarized in Table 3.

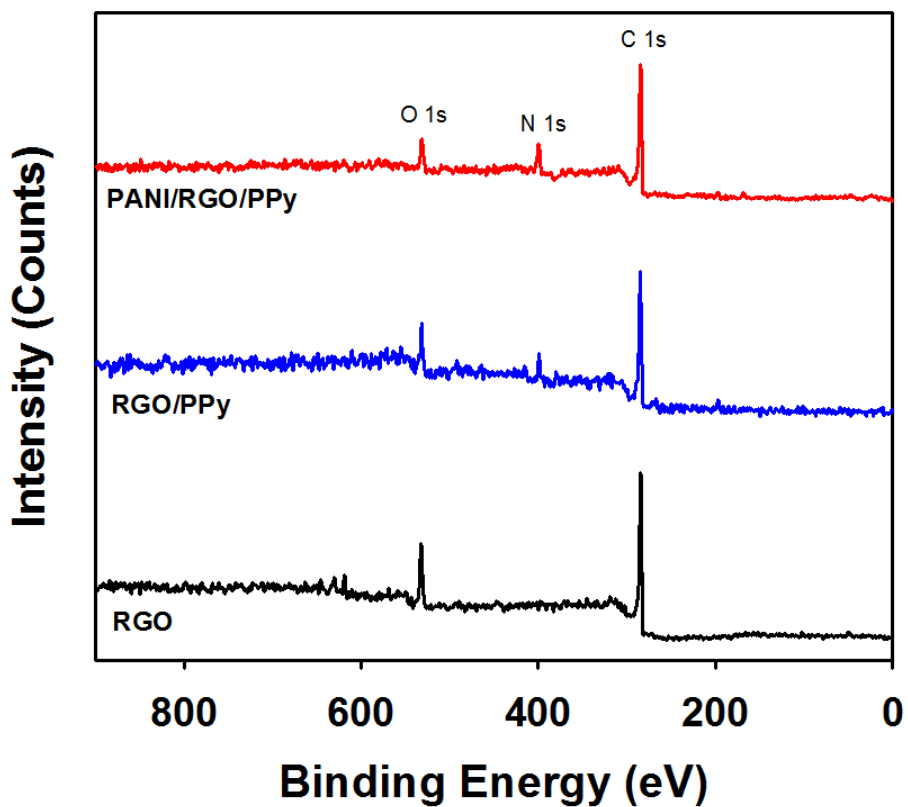


Figure 5. XPS spectra of PANI/RGO/PPy, RGO/PPy, and RGO (PPy: 0.3 wt%).

Table 3. The elemental composition of pristine RGO, pristine PPy, RGO/PPy and PANI/RGO/PPy composite (PPy: 0.3 wt%) as measured by XPS analysis. The values were calculated in atomic percent.

Sample	XPS atomic ratios of three atoms		
	C	N	O
Pristine RGO	85.9	0.53	13.57
Pristine PPy	71.44	10.7	17.87
RGO/PPy	75.35	3.97	20.68
PANI/RGO/PPy	78.06	12.24	9.69

3.3 Investigation of crystallinity

Figure 6a presents X-ray diffraction (XRD) patterns of RGO, RGO/PPy and PANI/RGO/PPy by fabrication procedure. Those for RGO exhibited a peak at 24.7° (d-spacing $\approx 3.60 \text{ \AA}$), which is in good agreement with that reported elsewhere [43]. Likewise, the RGO/PPy had a similar peak at 24.6° (d-spacing $\approx 3.61 \text{ \AA}$), meaning that RGO peak was conserved. The presence of PPy was vaguely observable because of the amorphous nature of PPy. The XRD pattern for PANI/RGO/PPy revealed representative peaks of pure PANI at 14.6° , 20.9° , 25.2° , and 27.0° (respective d-spacings ≈ 6.09 , 4.25 , 3.54 , and 3.31 \AA); these peaks correspond to the (011), (020), (200) and (121) crystal planes of PANI in the emeraldine salt form, respectively [44]. These peaks are an indication of the monoclinic space group $P2_1$ [45]. In addition, the RGO/PPy peak at 24.6° was absent from the XRD pattern for PANI/RGO/PPy, which suggests that the RGO sheets were completely covered with PANI nanofibers.

Figure 6b depicts an XRD pattern of PANI/RGO/PPy, as well as those for PANI/RGO and PANI. Compared with the patterns for PANI and PANI/RGO, that for PANI/RGO/PPy displays more intense peaks at 25° , but weaker peaks at 15° and 20° . It has been reported that the increment in the intensity of the peak at 25° originates from the face-to-face π - π stacking of

RGO planes and PANI nanofibers, which leads to the stretching of PANI nanofibers and an extended conjugation length, as well as enhancing the structural order and electrical conductivity [46]. Therefore, the enhanced electrical conductivity of PANI/RGO/PPy compared with PANI/RGO might be derived from the increased π - π interaction between the RGO/PPy and PANI. The same effect is observed in Figure 6c. The PANI/RGO/PPy with different weight ratio of PPy were investigated using the XRD patterns. In the Figure, the peak at 25° intensified as the increased concentration of PPy.

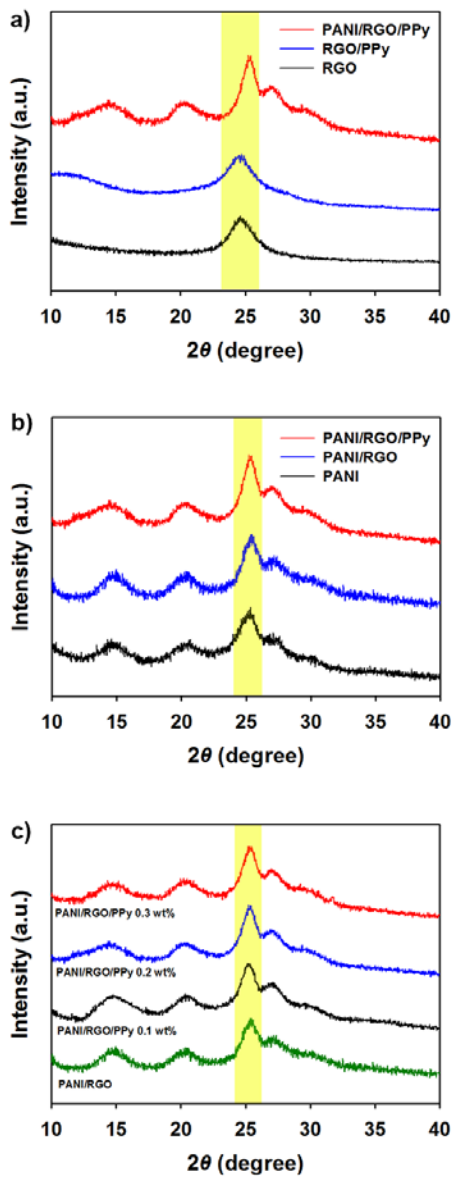


Figure 6. XRD patterns of PANI/RGO/PPy and (a) RGO/PPy and RGO; (b) PANI/RGO and PANI; (c) PANI/RGO and PANI/RGO/PPy with different PPy concentrations: 0.1, 0.2, and 0.3 wt%.

3.4. Investigation of electrochemical performance

The electrochemical performance of the PANI/RGO/PPy and constituent compounds was investigated using cyclic voltammetry (CV) and galvanostatic charge/discharge measurements. In the investigation, we used PANI/RGO/PPy with 0.3 wt% because of the prior investigation. Figure 7a presents the cyclic voltammograms for RGO, RGO/PPy, and PANI/RGO/PPy recorded at a scan rate of 10 mV s^{-1} . The CV curve of RGO illustrated rectangular shape, implying electrical double layer capacitance of graphene [47]. In contrast, the CV curves of RGO/PPy electrode had quasi-rectangular profiles with redox peaks corresponding to redox reactions of the PANI fibres [48]. The redox peaks were derived from the conversion of oxidation states of PPy [49]. The area under the CV curve of PANI/RGO/PPy electrode indicated that PANI/RGO/PPy capacitor yields improved specific capacitance at a given scan rate. Figure 7b exhibits the CV curves for PANI/RGO/PPy at different scan rates. The similar shapes with small redox peaks of the curves demonstrate stable capacitive behaviours of the PANI/RGO/PPy material.

Figure 7c shows typical galvanostatic charge/discharge curves for PANI/RGO/PPy, pure PANI, and RGO at a specific current of 0.5 A g^{-1} . The RGO illustrated a triangular-shape charge/discharge curve, reflecting that its

capacitance was majorly originated from electric double layer capacitance. However, the discharge curve of PANI/RGO/PPy demonstrated two voltage stages: 0.8–0.5 V and 0.45–0 V, respectively. The first stage is attributed to electric double layer capacitance and the second stage with a longer discharging duration is related with the combination of electric double layer and pseudo capacitance of PANI. The discharging curve of PANI/RGO/PPy was analogous to that of the pristine PANI. However, discharging time of PANI/RGO/PPy was much higher than pure PANI. Additionally, IR drop of PANI/RGO/PPy was much less than that of PANI. These results imply that the capacitance of PANI/RGO/PPy is much higher than that of PANI, whereas the internal resistance of the PANI/RGO/PPy is less than that of PANI. The specific capacitances of samples were precisely calculated based on the galvanostatic discharge curves. The specific capacitance of PANI/RGO/PPy was *ca.* 350 F g⁻¹, which is higher than that for PANI (*ca.* 300 F g⁻¹) and for RGO (*ca.* 10 F g⁻¹). This increment might be originated from the following three factors: 1) an enhanced available electroactive surface area of the PANI/RGO/PPy. The porous structure leads to the short path lengths for ions. [50]. Moreover, the spines of the urchin-like structure also produce the readily accessible electroactive surface area, an electron-transport pathway, and regions for charge diffusion [51], 2) the high electrical conductivity, and 3) the synergistic effect from the electric double layer and pseudocapacitances of RGO and PANI/PPy components [52].

Figure 7d displays the long-term cycle stability of PANI/RGO/PPy and PANI, which was characterized by a specific current of 0.5 A g^{-1} for 1000 cycles. The PANI/RGO/PPy cell retained *ca.* 78 % of the initial specific capacitance after 1000 cycles, whereas the PANI cell retained *ca.* 59 % of capacitance. This improvement is a result of the urchin-like structure given by the PPy, as well as the synergetic effects of the PANI and RGO.

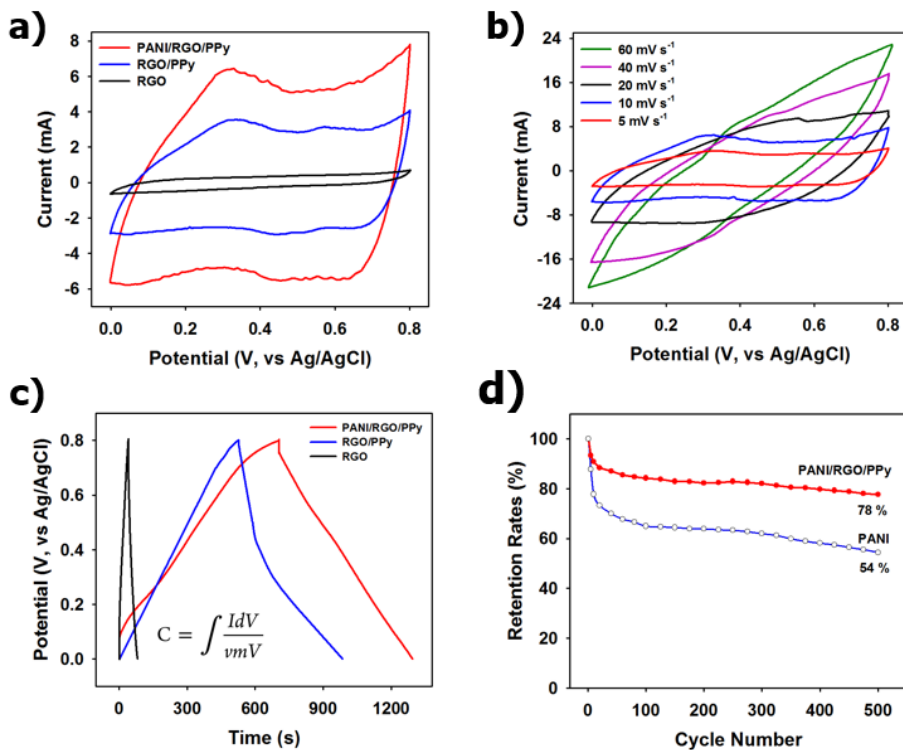


Figure 7. (a) CV curves for PANI/RGO/PPy, PANI/PPy, and RGO. (b) CV curves for PANI/RGO/PPy at different scan rates. (c) Galvanostatic charge/discharge profiles for PANI/RGO/PPy, PANI/PPy, and RGO. (d) Capacitance retention plot of PANI/RGO/PPy and PANI with cycle number (PPy: all 0.3 wt%).

Chapter 4. Conclusion

In summary, we have described the synthesis of multi-dimensional PANI/RGO/PPy using a simple in situ polymerization. Each step in the synthesis was confirmed by XPS and XRD analyses, and the morphology of the composite was characterized using SEM. The resulting PANI/RGO/PPy reflected an enhanced specific capacitance and favorable cycle stability compared with PANI, which originates from the urchin-like structure of PANI/PPy and high electrical conductivity. This work demonstrates that controlling shape of PANI can provide desired electrochemical properties. The addition of PPy can induce the urchin-like structure of PANI/PPy nanoballs, resulting in an increased specific surface area. This inexpensive self-assembly method would lead to the development of advanced devices with applications in energy storage systems.

References

- [1] Q. T. Qu, Y. Shi, S. Tian, Y. H. Chen, Y. P. Wu and R. Holze, *J. Power Sources*, **2009**, *194*, 1222.
- [2] J.-J. Li, Y.-X. Hu, M.-C. Liu, L.-B. Kong, Y.-M. Hu, W. H. Y.-C. Luo and L. Kang, *J. Alloy. Compd.*, **2016**, *656*, 138.
- [3] K.-W. Nam and K.-B. Kim, *J. Electrochem. Soc.*, **2002**, *149*, A346.
- [4] D. Kalpana, S. H. Cho, S. B. Lee, Y. S. Lee, R. Misra and N. G. Renganathan, *J. Power Sources*, **2009**, *190*, 587.
- [5] M. Toupin, T. Brousse and D. Belanger, *Chem. Mater.*, **2004**, *16*, 3184.
- [6] Y. Zhai, Y. Dou, D. Zhao, P. F. Fulvio, R. T. Mayes and S. Dai, *Adv. Mater.*, **2011**, *23*, 4828.
- [7] A. G. Pandolfo and A. F. Hollenkamp, *J. Power Sources*, **2006**, *157*, 11.
- [8] L. Hu, W. Chen, X. Xie, N. Liu, Y. Yang, H. Wu, Y. Yao, M. Pasta, H. N. Alshareef and Y. Cui, *ACS Nano*, **2011**, *5*, 8904.
- [9] Y. Cheng, S. Lu, H. Zhang, C. V. Varanasi and J. Liu, *Nano Lett.*, **2012**, *12*, 4206.
- [10] G. Yu, L. Hu, N. Liu, H. Wang, M. Vosgueritchian, Y. Yang, Y. Cui and Z. bao, *Nano Lett.*, **2011**, *11*, 4438.
- [11] X. Zhao, B. M. Sanchez, P. J. Dobson and P. S. Grant, *Nanoscale.*, **2011**, *3*, 839.
- [12] Y. Chen, X. Zhang, D. Zhang, P. Yu and Y. Ma, *Carbon*, **2011**, *49*, 573.

- [13] A. J. Roberts and R. C.T. Slade, *Electrochem. Acta*, **2010**, 55, 7460.
- [14] D. Wang, *J. Power Sources*, **2012**, 198, 416.
- [15] H. Jiang, P. S. Lee and C. Li, *Energy Environ. Sci.*, **2013**, 6, 41.
- [16] J. Jiang, Y. Li, J. Liu, X. Huang, C. Yuan and X. W. Lou, *Adv. Mater.*, **2012**, 24, 5166.
- [17] H. X. Bai, L. X. Zhang and Y. C. Zhang, *Mater. Lett.*, **2009**, 63, 82.
- [18] S. Chen, W. Xing, J. Duan, X. Hu and S. Z. Qiao, *J. Mater. Chem. A*, **2013**, 1, 2941.
- [19] H. Chen, J. Jiang, L. Zhang, H. Wan, T. Qi and D. Xia, *Nanoscale*, **2013**, 5, 8879.
- [20] T. Wu, J. Li, L. Hou and C. Yuan, *Electrochem. Acta*, **2012**, 81, 172.
- [21] B. Zhang, Y. Liu, Z. Huang, S. Oh, Y. Yu, Y.-W. Mai and J.-K. Kim, *J. Mater. Chem.*, **2012**, 22, 12133.
- [22] M. Huang, H. Yan, T. F. Heinz and J. Hone, *Nano Lett.*, **2010**, 10, 4074.
- [23] J. R. Miller, R. A. Outlaw and B. C. Holloway, *Electrochem. Acta*, **2011**, 56, 10443.
- [24] J. Yan, Z. Fan, T. Wei, W. Qian, M. Zhang and F. Wei, *Carbon*, **2010**, 48, 3825.
- [25] F. Du, D. Yu, L. Dai, S. Ganguli, V. Varshney and A. K. Roy, *Chem. Mater.*, **2011**, 23, 4810.
- [26] C. Yuan, H. B. Wu, Y. Xie and X. W. Lou, *Angew. Chem. Int. Edit.*, **2014**, 53, 1488.

- [27] W. Deng, X. Ji, Q. Chen and C. E. Banks, *RSC Adv.*, **2011**, *1*, 1171.
- [28] C.-C. Hu, K.-H. Chang, M.-C. Lin and Y.-T. Wu, *Nano Lett.*, **2006**, *6*, 2690.
- [29] R. B. Rakhi, W. Chen, D. Cha and H. N. Alshareef, *J. Mater. Chem.*, **2011**, *21*, 16197.
- [30] J. Heinze, B. A. Frontana-Urbe and S. Ludwigs, *Chem. Rev.*, **2010**, *110*, 4724.
- [31] D. Li, J. Huang and R. B. Kaner, *Acc. Chem. Res.*, **2009**, *42*, 135.
- [32] M. Kim, C. Lee and J. Jang, *Adv. Funct. Mater.*, **2014**, *24*, 2489.
- [33] K. Lee, S. Cho, S. Heum Park, A. J. Heeger, C.-W. Lee and S.-H. Lee, *Nature*, **2006**, *441*, 65.
- [34] B. H. Lee, S. H. Park, H. Back and K. Lee, *Adv. Funct. Mater.*, **2011**, *21*, 487.
- [35] S. Cho, M. Kim, J. S. Lee, J. Jang, *ACS Appl. Mater. Interfaces*, **2015**, *7*, 22301.
- [36] S. Lee, C.-M. Yoon, J.-Y. Hong, J. Jang, *J. Mater. Chem. C*, **2014**, *2*, 6010.
- [37] J.-Y. Hong, S. O. Jeon, J. Jang, K. Song, S. H. Kim, *Org. Electron.*, **2013**, *14*, 979.
- [38] K. Lee, S. Cho, M. Kim, J. Kim, J. Ryu, K.-Y. Shin, J. Jang, *J. Mater. Chem. A*, **2015**, *3*, 19018.
- [39] S. Cho, J. S. Lee, J. Jun, S. G. Kim, J. Jang, *Nanoscale*, **2014**, *6*, 15181.

- [40] Q. Zhou, Y. Li, L. Huang, C. Li, G. Shi, *J. Mater. Chem. A*, **2014**, *2*, 17489.
- [41] M. Li, X. Huang, C. Wu, H. Xu, P. Jiang, T. Tanaka, *J. Mater. Chem.*, **2012**, *22*, 23477.
- [42] J.-Y. Hong, H. Yoon, J. Jang, *Small*, **2010**, *6*, 679.
- [43] I. K. Moon, J. Lee, H. Lee, *Chem. Commun.*, **2011**, *47*, 9681.
- [44] H. Ding, Y. Long, J. Shen, M. Wan, *J. Phys. Chem. B*, **2010**, *114*, 115.
- [45] L. Zhang, M. Wan, Y. Wei, *Macromol. Rapid Commun.*, **2006**, *27*, 366.
- [46] M. Kim, C. Lee, J. Jang, *Adv. Funct. Mater.*, **2013**, *24*, 2489.
- [47] H.-P. Cong, X.-C. Ren, P. Wang, S.-H. Yu, *Energ. Environ. Sci.*, **2013**, *6*, 1185.
- [48] D.-W. Wang, F. Li, J. Zhao, W. Ren, Z.-G. Chen, J. Tan, Z.-S. Wu, I. Gentle, G. Q. Lu, H.-M. Cheng, *ACS Nano*, **2009**, *3*, 1745.
- [49] J. Zhu, Y. Xu, J. Wang, J. Wang, Y. Bai, X. Du, *Phys. Chem. Chem. Phys.*, **2015**, *17*, 19885.
- [50] H. Chen, J. Jiang, L. Zhang, H. Wan, T. Qi, D. Xia, *Nanoscale*, **2013**, *5*, 8879.
- [51] Y. Li, Q. Zhang, X. Zhao, P. Yu, L. Wu, D. Chen, *J. Mater. Chem.*, **2012**, *22*, 1884.
- [52] J. Ma, Q. Cheng, V. Pavlinek, P. Saha, C. Li, *New J. Chem.*, **2013**, *37*, 722.

초 록

본 실험에서는 폴리피롤을 기핵제로 사용하여 자체안정화 분산중합을 통해 성게 구조의 폴리아닐린 (직경 약 500 nm)을 제조하고 이 구조와 그래핀의 복합체를 형성하여 슈퍼커패시터 전극으로 활용하였다. 폴리피롤 나노 입자 (직경 약 100 nm)는 그래핀의 뭉침 현상을 억제하고 폴리아닐린 중합의 핵 기능을 하여 높은 표면적을 가진 성게 모양의 전도성 고분자 구조를 형성하였다. 또한 그래핀은 폴리아닐린의 뭉침 현상을 억제하고 전자 전달 통로와 높은 안정성을 제공하는 기능을 하였다. 이러한 구조를 통하여 제조한 복합체의 전기전도도 또한 약 24 S cm^{-1} 까지 증가하였다. 성게 모양 폴리아닐린/폴리피롤과 그래핀의 복합체를 슈퍼커패시터 전극으로 활용하였으며, 그 결과 0.5 A g^{-1} 에서 약 350 A g^{-1} 의 커패시턴스와 1000회에서 78 %의 커패시턴스 보존 효과를 얻을 수 있었다. 이 논문은 슈퍼커패시터 전극을 위한 성게 모양의 전도성 고분자 물질을 제조하는 간단한 방법을 제공하는 데 목적이 있다.

주요어 : 폴리아닐린, 그래핀, 폴리피롤, 슈퍼커패시터

학번 : 2014-20629